

# Cavity exciton-polaritons in two-dimensional semiconductors from first principles

Dino Novko<sup>1,2</sup> and Vito Despoja<sup>1,2,\*</sup>

<sup>1</sup>*Institute of Physics, Bijenička 46, 10000 Zagreb, Croatia*

<sup>2</sup>*Donostia International Physics Center (DIPC),  
P. Manuel de Lardizabal, 4, 20018 San Sebastián, Spain*

Two-dimensional (2D) semiconducting microcavity, where exciton-polaritons can be formed, constitutes a promising setup for exploring and manipulating various regimes of light-matter interaction. Here, the coupling between 2D excitons and metallic cavity photons is studied by using first-principles propagator technique. The strength of exciton-photon coupling is characterised by its Rabi splitting to two exciton-polaritons, which can be tuned by cavity thickness. Maximum splitting of 128 meV is achieved in phosphorene cavity, while remarkable value of about 440 meV is predicted in monolayer hBN device. The obtained Rabi splittings in WS<sub>2</sub> microcavity are in excellent agreement with the recent experiments. Present methodology can aid in predicting and proposing potential setups for trapping robust 2D exciton-polariton condensates.

The interplay between cavity photons and matter can result in formation of hybrid polarization-photon modes, commonly called polaritons [1]. Due to their dual light-matter nature, these bosonic quasiparticles are enriched with exceptional physical properties, such as small effective mass and nonlinearity, absent in the matter outside the optical cavity. As such, polaritons are expected to show exotic physical phenomena like light-induced superconductivity [2, 3], Bose-Einstein condensation [4–6], polariton superfluidity [7], and quantized vortices [8]. Ideal platforms for studying strong light-matter interactions are gapped systems, such as semiconductors [6, 9] or molecules [10], placed in microcavity devices, where exciton-polaritons are formed. Cavity exciton-polaritons, showing a plethora of quantum effects, are routinely observed in bulk [11–14] and quantum well systems [9, 15], e.g., devised from GaAs [9].

Two-dimensional (2D) materials, such as semiconducting monolayers, thin heterostructures and films, are even more attractive than their bulk counterparts, due to the reduced Coulomb screening and the corresponding large exciton binding energies [16–23] that enable formation of well-defined exciton-polaritons even at room temperatures [24]. The first 2D exciton-polariton were realized in monolayer of transition metal dichalcogenide (TMD) MoS<sub>2</sub>, where Rabi splitting between exciton and cavity photon of  $\sim 50$  meV was observed [25]. Further photoluminescence studies showed clear anticrossing behaviour and splitting of exciton-polariton in other 2D TMD cavity devices, e.g., in MoSe<sub>2</sub> [26], WS<sub>2</sub> [27], WSe<sub>2</sub> [28, 29], and in MoSe<sub>2</sub>-WSe<sub>2</sub> heterostructure [30]. In addition, real-space imaging of exciton-polaritons was done by means of near-field scanning optical microscopy for WSe<sub>2</sub> thin films [31]. These TMD semiconductor microcavities are especially appealing due to their charge tunability, coupled spin and valley degrees of freedom, as well as ability to form heterostructures, and are thus able to display valley-polarized exciton-polaritons [32], polaron-polaritons [33], and interlayer exciton-polaritons [30].

Despite this enormous interest in exciton-polaritons

and semiconductor microcavity devices, a complementary microscopic theories that are able to scrutinize the cavity photon-exciton coupling on the quantitative and predictive level are still rare. In addition, the majority of the microscopic descriptions are based on simple model Hamiltonians describing exciton-photon interactions in microcavity [34–39]. Recently, a more rigorous *ab initio* theoretical description of exciton-polaritons in TMD microcavity was provided in the framework of the quantum-electrodynamical Bethe-Salpeter equation [40], where the excitons are calculated from first-principles Bethe-Salpeter equation, and the electromagnetic field is described by quantized photons. However, the coupling between excitons and photons is left to be arbitrary. This study showed how excitonic optical activity and energetic ordering can be controlled via cavity size, light-matter coupling strength, and dielectric environment.

Here, we present a fully quantitative theory of 2D exciton-polaritons embedded in plasmonic microcavity that is able to analyze and predict light-matter coupling strengths for various cavity settings. We study cavity exciton-polaritons in three prototypical two-dimensional single-layer semiconductors, i.e., single-layer black phosphorus or phosphorene (P<sub>4</sub>), WS<sub>2</sub>, and hexagonal boron nitride hBN. The results show a clear Rabi splitting between 2D exciton and cavity photon modes as well as high degree of tunability of Rabi (light-matter) coupling  $\Omega$  as a function of microcavity thickness. In the case of WS<sub>2</sub>, for the usual experimental setup where cavity size is around  $d \sim 1 \mu\text{m}$  we obtain splittings of  $\Omega \sim 42$  meV and  $\Omega \sim 64$  meV for principal and second cavity modes, in line with the experiments [25, 27]. Also, in all cases larger coupling strengths  $\Omega$  are found for larger photon confinements when  $d < 1 \mu\text{m}$  as well as for higher cavity modes  $n$ . Interestingly, the ultraviolet (UV) exciton in hBN shows a very strong exciton-cavity photon coupling of about  $\sim 440$  meV and a possibility of Bose-Einstein condensation.

In this work both excitons and photons are described by bosonic propagators  $\sigma$  and  $\Gamma$ , respectively, which are

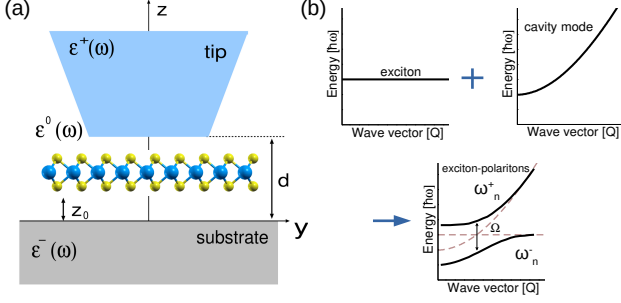


FIG. 1: (a) The schematic of a microcavity device. The 2D crystals described by optical conductivity  $\sigma_\mu(\omega)$  is inserted in microcavity which consists of substrate, dielectric media and tip described by macroscopic dielectric functions  $\epsilon^-(\omega)$ ,  $\epsilon^0(\omega)$  and  $\epsilon^+(\omega)$ , respectively. (b) The interaction between 2D exciton and cavity mode results in creation of exciton-polaritons. The coupling strength measure is Rabi splitting  $\Omega$ .

derived from first principles. The 2D crystal optical conductivity  $\sigma$  is calculated using *ab initio* RPA+ladder method [41], and propagator of cavity photons  $\Gamma$  is derived by solving the Maxwell's equations for planar cavity described by local dielectric function  $\epsilon$  (see Supplemental Material [42]). The exciton-photon coupling is achieved by dressing the cavity-photon propagator  $\Gamma$  with excitons at the RPA level. Thus obtained results are therefore directly comparable with the experiments. As illustrated in Fig. 1(a) the microcavity device consists of substrate, tip and dielectric media in between, described by local dielectric functions  $\epsilon^+$ ,  $\epsilon^-$  and  $\epsilon^0$ , respectively. The 2D semiconducting crystal defined by optical conductivity  $\sigma_\mu(\omega)$  is immersed in a dielectric media at a height  $z_0$  relative to the substrate. The substrate occupy region  $z < 0$ , tip occupy region  $z > d$ , and dielectric media occupy region  $0 < z < d$ . In such semiconducting microcavity setup the coupling between the exciton and cavity photon is expected to result in the splitting of exciton-polariton to the lower and upper polariton branches (LPB and UPB), which we shall refer as  $\omega_n^-$  and  $\omega_n^+$ , respectively [see Fig. 1(b)].

The quantity from which we extract the information about the electromagnetic modes in microcavity setup is electrical field propagator  $\mathcal{E}_{\mu\nu}$  which, by definition [43], propagates the electrical field produced by point oscillating dipole  $\mathbf{p}_0 e^{-i\omega t}$ , i.e.  $\mathbf{E}(\omega) = \mathcal{E}(\omega)\mathbf{p}^0$ . Assuming that the 2D crystal, substrate and tip satisfy planar symmetry (in  $x-y$  plane) the propagator  $\mathcal{E}$  in  $z = z_0$  plane satisfies matrix equation

$$\mathcal{E}(\mathbf{Q}, \omega) = \mathbf{\Gamma}(\mathbf{Q}, \omega) + \mathbf{\Gamma}(\mathbf{Q}, \omega)\sigma(\omega)\mathcal{E}(\mathbf{Q}, \omega)$$

as illustrated by Feynman diagrams in Fig. 2(a) (see also Sec. S1.A in Ref. [42]). Here  $\mathbf{\Gamma} = \mathbf{\Gamma}^0 + \mathbf{\Gamma}^{sc}$  represents the propagator of electrical field, in absence of 2D crystal, i.e. when  $\sigma = 0$ . The propagator  $\mathbf{\Gamma}^0$  represents the “free”

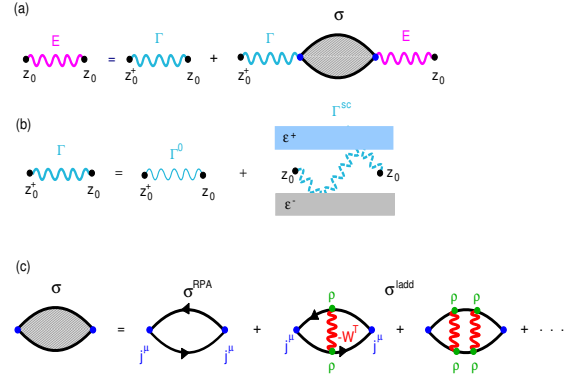


FIG. 2: (a) Dyson's equation for the propagator of the electrical field  $\mathcal{E}$  in a microcavity device. (b) Propagator of the electrical field  $\mathbf{\Gamma} = \mathbf{\Gamma}^0 + \mathbf{\Gamma}^{sc}$ , in absence of 2D crystal (i.e., when  $\sigma_\mu = 0$ ). (c) Perturbative expansion of optical conductivity  $\sigma_\mu(\omega)$ . Blue dots represent the current vertices  $j^\mu$ , green dots represent the charge vertices  $\rho$  and red wavy lines represent the screened Coulomb interaction  $W^T$ .

electrical field and the propagator of scattered electrical field  $\mathbf{\Gamma}^{sc}$  results in multiple reflections at the microcavity interfaces, as illustrated in Fig. 2(b). In order to simplify the interpretation of the results we suppose that the dielectric media is vacuum ( $\epsilon^0 = 1$ ), and we suppose that tip and substrate are made of the same material ( $\epsilon^- = \epsilon^+ = \epsilon$ ). In order to support well-defined cavity modes, these materials should be highly reflective in the exciton frequency region  $\omega \approx \omega_{ex}$ , which is satisfied if  $\omega_{ex} < \omega_p$ , where  $\omega_p$  is the bulk plasmon frequency. For the  $\text{P}_4$  and  $\text{WS}_2$  monolayers where exciton energies are  $\hbar\omega_{ex} < 3.0\text{eV}$ , we chose that the substrate and tip are made of silver ( $\omega_p \approx 3.6\text{eV}$ ). On the other hand, for the single-layer hBN where exciton energy is  $\hbar\omega_{ex} = 5.67\text{eV}$  we chose aluminium ( $\omega_p \approx 15\text{eV}$ ). Both silver and aluminium macroscopic dielectric functions  $\epsilon(\omega)$  are determined as well from the first principles (see Ref. [42]). As an example, the intensity of electromagnetic modes ( $-\text{Im}\Gamma_x$ ) in silver microcavity is shown in Fig. S2 in Ref. [42]. Figure 2(c) shows the perturbative expansion of optical conductivity  $\sigma_\mu(\omega) = \sigma_\mu^{RPA}(\omega) + \sigma_\mu^{ladd}(\omega)$ , where  $\sigma^{RPA}$  is the RPA optical conductivity [44, 45], while the ladder optical conductivity is  $\sigma^{ladd} = \frac{i}{\omega S} j\mathcal{K}j^*$ , where  $S$  is a normalization surface and  $j$  are the current vertices. The 4-points polarizability  $\mathcal{K}$  satisfies the Dyson equation [42] in which the Bethe-Salpeter-Fock kernel  $\Phi^F$  enters [46–50]. The electron energies are corrected using the GW method so that the present approach is equivalent to time-dependent screened Hartree-Fock approximation [46–51]. For more details see Secs. S1.B and S2.B in Ref. [42]. Without cavity photons, the total optical absorption  $\text{Re}\sigma_x(\omega)$  in  $\text{P}_4$  and hBN is characterized with the strong excitons appearing at  $\hbar\omega_{ex} = 1.45\text{eV}$  and  $\hbar\omega_{ex} = 5.67\text{eV}$ , respectively. In addition, the absorption spectrum  $\text{Re}\sigma_x(\omega)$  in  $\text{WS}_2$  shows the two spin-

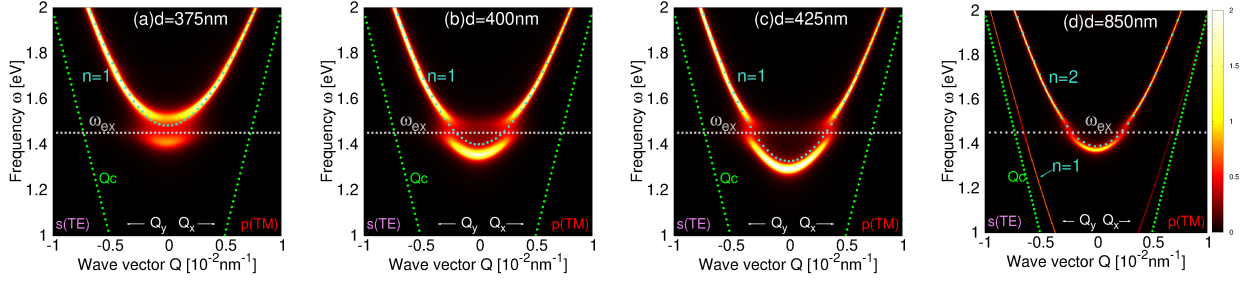


FIG. 3: The intensities of electromagnetic modes ( $-\text{Im}\mathcal{E}_{xx}$ ) showing the hybridisation between silver cavity mode  $n = 1$  (magenta dotted) and  $P_4$  exciton (white dotted) for various cavity sizes: (a)  $d = 375$  nm, (b)  $d = 400$  nm, and (c)  $d = 425$  nm, where  $z_0 = d/2$ . (d) The hybridisation between cavity mode  $n = 2$  and  $P_4$  exciton in cavity of thickness  $d = 850$  nm and  $z_0 = d/4$ .

orbit splitted A and B excitons at  $\hbar\omega_{ex}^A = 2.1$  eV and  $\hbar\omega_{ex}^B = 2.46$  eV [42].

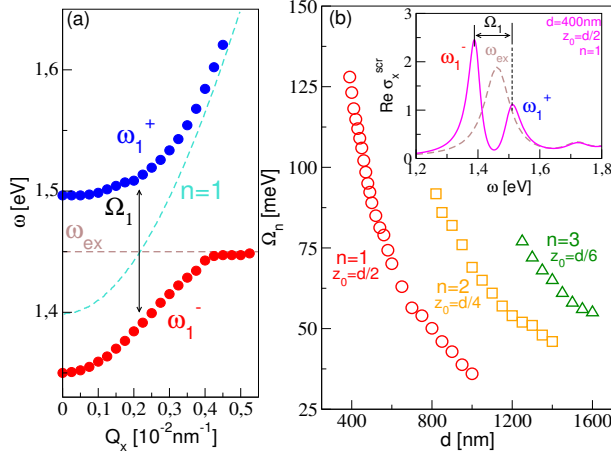


FIG. 4: (a) The dispersion relations of exciton-polaritons  $\omega_1^-$  and  $\omega_1^+$  (dots) for  $P_4$  in silver microcavity of thickness  $d = 400$  nm and  $z_0 = d/2$ . Dashed lines show unperturbed modes. (b) The Rabi splittings  $\Omega_n = \omega_n^+ - \omega_n^-$  versus cavity thickness  $d$  for  $n = 1$  (red circles),  $n = 2$  (orange squares) and  $n = 3$  (green triangles) cavity modes, where  $z_0 = d/2$ ,  $z_0 = d/4$  and  $z_0 = d/6$ , respectively. The inset shows  $\text{Re}\sigma_x^{\text{scr}}$  before (brown dashed) and after (solid magenta) the  $P_4$  is inserted in the cavity, where  $d = 400$  nm,  $z_0 = d/2$  and  $Q_x = 0.00217$  nm $^{-1}$  (momentum for which exciton crosses the  $n = 1$  mode).

Figures 3(a), 3(b), and 3(c) show the modifications of the  $n = 1$  cavity mode intensity after the single-layer  $P_4$  is inserted in the middle  $z_0=d/2$  ( $n = 1$  antinodal plane) of the silver cavity, where the cavity sizes are  $d = 375$  nm,  $d = 400$  nm and  $d = 425$  nm, respectively. White and turquoise dotted lines denote the  $P_4$  exciton and unperturbed cavity mode  $n = 1$ , respectively. For  $d = 375$  nm, just before the  $n = 1$  cavity mode crosses the exciton, a significant part of the  $n = 1$  mode spectral weight is transferred below the exciton energy. By increasing the cavity size, i.e. for  $d = 400$  nm and  $d = 425$  nm, the exciton crosses the  $n = 1$  mode, which results in

the intensity weakening and band-gap opening in the intersection area. This behaviour enables creation of exciton-polariton condensate, as experimentally verified in Refs. [6, 13–15, 29]. By changing the cavity thickness, the exciton can interact also with the higher cavity modes. Figure 3(d) shows the modifications of  $n = 2$  mode intensity, where the cavity thickness is  $d = 850$  nm and  $P_4$  is chosen to be located at  $z_0 = d/4$  nm ( $n = 2$  antinodal plane). The exciton significantly weakens the intensity of  $n = 2$  mode in the intersection area, however, here the avoided crossing behaviour is not clearly noticeable in comparison with the exciton coupled to the 1st cavity mode.

The dispersion relation of exciton-polaritons  $\omega_n^-$  and  $\omega_n^+$  (hybridised cavity photon-exciton modes), as the one shown in Fig. 4(a), can be precisely determined by following the splitted maxima in induced current  $j_\mu = \sigma_\mu^{\text{scr}} E_\mu$  driven by external (bare) field  $E_\mu e^{-i\omega t}$ , where the screened optical conductivity is  $\sigma_\mu^{\text{scr}} = [1 - \Gamma\sigma]_\mu^{-1} \sigma_\mu$ . The inset of Figure 4(b) shows the  $\text{Re}\sigma_x^{\text{scr}}$  before (brown dashed) and after (solid magenta) the  $P_4$  is inserted in the middle of the cavity of thickness  $d = 400$  nm. The splitting of exciton  $\hbar\omega_{ex}$  to exciton-polaritons  $\omega_1^-$  and  $\omega_1^+$  can be clearly seen. The exciton-photon binding strength can be determined from the Rabi splitting defined as difference  $\Omega_n = \omega_n^+ - \omega_n^-$  for wave vector  $\mathbf{Q}$  and for which the bare cavity modes  $n = 1, 2, 3, \dots$  crosses the exciton  $\hbar\omega_{ex}$ . Figure 4(a) shows the dispersion relations of plasmon-polaritons  $\omega_1^-$  and  $\omega_1^+$  obtained by following the splitted maxima in  $\text{Re}\sigma_x^{\text{scr}}$  for different wave vectors  $Q_x$ ,  $d = 400$  nm and  $z_0 = d/2$ . The clear anticrossing behaviour and Rabi splitting of  $\Omega_1 = 123$  meV indicates strong interaction between exciton and  $n = 1$  cavity photon. Red circles, yellow squares and green triangles in Fig. 4(b) show the Rabi splittings  $\Omega_n$  for  $n = 1$ ,  $n = 2$  and  $n = 3$ , respectively, versus cavity thickness  $d$ . The maximum Rabi splittings of  $n$ th mode  $\Omega_n^{\text{max}}$  are achieved when  $z_0 = d/2$  and for  $d$  chosen so that  $n$ th mode just starts to cross the exciton energy  $\hbar\omega_{ex}$ . All three modes show strong coupling with exciton that results in the

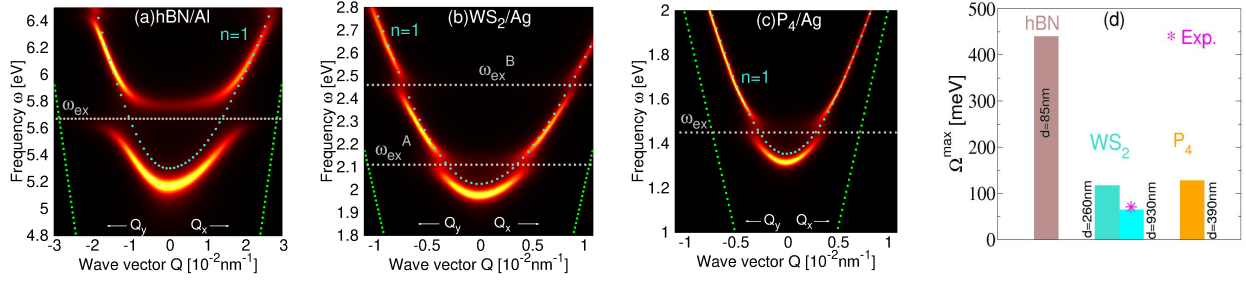


FIG. 5: The intensity of electromagnetic modes ( $-\text{Im}\mathcal{E}_{xx}$ ) showing the hybridisation between cavity mode  $n = 1$  (magenta dotted) and (a) hBN exciton (white dotted) in aluminium cavity of thickness  $d = 90$  nm, (b) the  $\text{WS}_2$  A and B excitons in silver cavity of thickness  $d = 260$  nm, and (c) the  $\text{P}_4$  exciton in silver cavity of thickness  $d = 415$  nm. The  $z_0 = d/2$  in all cases. (d) Summary of the obtained Rabi splittings in studied systems. The experimental value for  $\text{WS}_2$  microcavity is from Ref. [27].

maximum splittings of  $\Omega_1^{\text{max}} = 128$  meV,  $\Omega_2^{\text{max}} = 92$  meV and  $\Omega_3^{\text{max}} = 77$  meV for  $d = 390$  nm,  $d = 820$  nm and  $d = 1250$  nm, respectively. For larger  $d$  the cavity modes cross exciton at a greater angle and the splitting decreases. A decrease of  $\Omega_n^{\text{max}}$  as  $n$  increases confirms a confinement hypothesis; as  $n$  increases the cavity photon modes crosses the exciton for larger  $d$ , and photon becomes less confined while the coupling is reduced. Thus, the coupling will be stronger as the thickness  $d$  at which the crossing between  $n$ th mode and exciton occurs is getting smaller.

The above criterion is met by excitons with higher excitation energy, such as for instance the UV exciton in the hBN single layer. Since in the same UV frequency region the cavity should be highly reflective (i.e.,  $\omega_p > \omega_{ex}$ ), the appropriate cavity for hBN layer can be made of aluminium with  $\omega_p \approx 15$  eV. Figure 5(a) shows the modification of aluminium  $n = 1$  cavity mode intensity after the hBN monolayer is inserted in the middle of cavity of thicknesses  $d = 90$  nm. The dotted lines show the unperturbed cavity mode  $n = 1$  and the hBN exciton. The strong exciton-photon interaction results in strong modification of the  $n = 1$  cavity mode, band-gap opening and Rabi splitting of  $\Omega_1 = 400$  meV. The maximum Rabi splitting of  $\Omega_1^{\text{max}} = 440$  meV is achieved for  $d = 85$  nm. This large exciton-polariton band gap and Rabi splitting suggest a possibility of experimental realization of robust exciton-polariton condensate in the cavity setup.

The 2D exciton-polaritons are experimentally studied mostly in various TMDs where the measured Rabi splittings of  $\Omega = 46$  meV,  $\Omega = 26$  meV, and  $\Omega = 20$  meV are found in  $\text{MoS}_2$  [25],  $\text{WSe}_2$  [28], and  $\text{MoSe}_2$  [26]. For  $\text{WS}_2$  the experimentally measured splittings are around 20 – 70 meV for  $d > 1 \mu\text{m}$ , depending on the precise cavity size [27]. In Fig. 5(b) we show the modification of the silver  $n = 1$  cavity mode intensity when the  $\text{WS}_2$  monolayer is inserted in the middle of microcavity of thickness  $d = 260$  nm. The unperturbed  $n = 1$  mode as well as the A and B excitons of bare  $\text{WS}_2$  are also denoted by dotted lines. Both excitons significantly per-

turb the  $n = 1$  mode providing the Rabi splittings of  $\Omega_1^A = 117$  meV and  $\Omega_1^B = 103$  meV. For comparison, Fig. 5(c) shows the modification of  $n = 1$  mode intensity when  $\text{P}_4$  is inserted in silver microcavity for the same conditions as in  $\text{WS}_2$  microcavity presented in Fig. 5(b);  $n = 1$  minimum is 100 meV below the exciton. The cavity thickness is  $d = 415$  nm and  $z_0 = d/2$ . Interestingly, the achieved Rabi splitting is here also  $\Omega_1 = 117$  meV, even though according to confinement hypothesis, the A exciton, which is confined in smaller cavity, is expected to split more. However, the A exciton in  $\text{WS}_2$  has smaller oscillatory strength than  $\text{P}_4$  exciton [cf. Figs. S4(a) and S5(b) in Ref. [42]] so that the binding is weaker and the two effects cancel.

Finally, in Fig. 5(d) we compare the maximum splittings of exciton-polaritons  $\Omega^{\text{max}}$  for the three semiconducting microcavities, summarizing the different regimes of exciton-cavity photon coupling strengths in these materials. For  $\text{WS}_2$  microcavity we additionally present the results for the experimentally measured value of cavity size, i.e.,  $d = 930$  nm [27], when exciton interacts with  $n = 2$  cavity mode. The corresponding value of  $\Omega_2^A = 64$  meV shows an excellent agreement with the experiment [27]. For the same cavity thickness, splitting of the  $n = 1$  cavity mode and the  $\text{WS}_2$  A exciton is  $\Omega_1^A = 42$  meV.

In summary, we have studied the interaction strengths between cavity photons and excitons in various 2D semiconducting crystals by means of rigorous *ab initio* methodology. It is shown that insertion of 2D crystals into a metallic microcavity significantly modifies the photon dispersion. For instance, the band gap opening and Rabi splitting as high as  $\Omega = 440$  meV was obtained for hBN cavity device. This opens a possibility of experimental realization of the robust 2D exciton-polariton condensate. Moreover, the exciton-photon interaction strongly depends on photon confinement, which was shown to be adjustable by the cavity thickness  $d$ . The results of exciton-polariton splitting in  $\text{WS}_2$  cavity device show a good agreement with recent experiments



and suggest higher photon confinements with decreasing cavity size at which stronger photon-matter coupling should be achieved. In order reach this stronger binding we suggest an experimental setup consisting of tunable submicrometer cavity (such as AFM-tip and substrate) tuned so that the principal photon cavity mode coincide with the exciton energy, e.g. as in Fig.4(b).

The authors acknowledge financial support from European Regional Development Fund for the “QuantiXLie Centre of Excellence” (Grant KK.01.1.1.01.0004) and “Center of Excellence for Advanced Materials and Sensing Devices” (Grant No. KK.01.1.1.01.0001), as well as from Croatian Science Foundation (Grant no. IP-2020-02-5556 and Grant No. UIP-2019-04-6869). Computational resources were provided by the Donostia International Physic Center (DIPC) computing center.

---

\* Electronic address: [vdespoja@ifs.hr](mailto:vdespoja@ifs.hr)

- [1] D. N. Basov, Ana Asenjo-Garcia, P. James Schuck, Xiaoyang Zhu and Angel Rubio, *Nanophotonics* **10** 549 (2021)
- [2] F. Schlawin, A. Cavalleri, and D. Jaksch, *Phys. Rev. Lett.* **122**, 133602 (2019).
- [3] J. B. Curtis, Z. M. Raines, A. A. Allocca, M. Hafezi, and V. M. Galitski, *Phys. Rev. Lett.* **122**, 167002 (2019).
- [4] J. Kasprzak, M. Richard, S. Kundermann *et al.*, *Nature* **443**, 409 (2006).
- [5] R. Balili, V. Hartwell, D. Snoke, L. Pfeiffer, and K. West, *Science* **316**, 1007 (2007).
- [6] H. Deng, H. Haug, and Y. Yamamoto, *Rev. Mod. Phys.* **82**, 1489 (2010).
- [7] A. Amo, J. Lefrère, Simon Pigeon *et al.*, *Nature Phys.* **5**, 805 (2009).
- [8] K. G. Lagoudakis, M. Wouters, M. Richard *et al.*, *Nature Phys.* **4**, 706 (2008).
- [9] C. Weisbuch, M. Nishioka, A. Ishikawa, and Y. Arakawa, *Phys. Rev. Lett.* **69**, 3314(1992).
- [10] R. F. Ribeiro, L. A. Martínez-Martínez, M. Du, J. Campos-Gonzalez-Angulo, and J. Yuen-Zhou, *Chem. Sci.* **9**, 6325 (2018).
- [11] S. Christopoulos, G. Baldassarri Höger von Högersthal, A. J. D. Grundy *et al.*, *Phys. Rev. Lett.* **98**, 126405 (2007).
- [12] J. J. Baumberg, A. V. Kavokin, S. Christopoulos *et al.*, *Phys. Rev. Lett.* **101**, 136409 (2008).
- [13] S. Zhang, J. Chen, J. Shi *et al.*, *ACS Photonics* **7** 327 2020.
- [14] W. Bao, X. Liu, F. Xue *et al.*, *PNAS* **116**, 20274 (2019).
- [15] T. Horikiri, T. Byrnes, K. Kusudo, N. Ishida, Y. Matsuo, Y. Shikano, A. Löffler, S. Höfling, A. Forchel, and Y. Yamamoto, *Phys. Rev B* **95**, 245122 (2017).
- [16] A. Ramasubramaniam, *Phys. Rev. B* **86**, 115409 (2012)
- [17] Y. Li, A. Chernikov, X. Zhang, A. Rigosi, H. M. Hill, A. M. van der Zande, D. A. Chenet, En-Min Shih, J. Hone, and T. F. Heinz, *Phys. Rev. B* **90**, 205422 (2014)
- [18] D. Y. Qiu, F. H. Jornada, S. G. Louie, *Phys. Rev. Lett.* **111**, 216805 (2013)
- [19] Y. Lin, X. Ling, L. Yu, S. Huang, Allen L. Hsu, Yi-Hsien Lee, J. Kong, M. S. Dresselhaus, and T. Palacios, *Nano Lett.* **14**, 5569 (2014)
- [20] J. Yan, K. W. Jacobsen, K. S. Thygesen, *Phys. Rev. B* **86**, 045208 (2012)
- [21] F. Ferreira and R. M. Ribeiro, *Phys. Rev B* **96**, 115431 (2017)
- [22] C. E. P. Villegas, A. S. Rodin, A. C. Carvalho, and A. R. Rocha, *Physical Chemistry Chemical Physics* **18** (40) (2016)
- [23] X. Wang, A. M. Jones, K. L. Seyler, V. Tran, Yichen Jia, Huan Zhao, Han Wang, Li Yang, Xiaodong Xu and Fengnian Xia, *Nature Nanotechnology* **10**, 517 (2015)
- [24] T. Low, A. Chaves, J. D. Caldwell, A. Kumar, N. X. Fang, P. Avouris, T. F. Heinz, F. Guinea, L. Martin-Moreno and Frank Koppens, *Nature Materials* **16**, 182 (2017)
- [25] Xiaoze Liu, Tal Galfsky, Zheng Sun, Fengnian Xia, Erhchen Lin, Yi-Hsien Lee, Stéphane Kéna-Cohen and Vinod M. Menon, *Nature Photonics* **9** (1) (2014)
- [26] S. Dufferwiel, S. Schwarz, F. Withers, A.A.P. Trichet, F. Li, M. Sich, O. Del Pozo-Zamudio, C. Clark 4, A. Nalitov, D.D. Solnyshkov, G. Malpuech, K.S. Novoselov, J.M. Smith, M.S. Skolnick, D.N. Krizhanovskii and A.I. Tartakovskii, *Nature Communications* **6**, 8579 (2015)
- [27] L. C. Flatten, Z. He, D. M. Coles, A. A. P. Trichet, A. W. Powell, R. A. Taylor, J. H. Warner and J. M. Smith, *Sci. Rep.* **6**, 33134 (2016).
- [28] S. Dufferwiel, T.P. Lyons, D.D. Solnyshkov, A.A.P. Trichet, A. Catanzaro, F. Withers, G. Malpuech, J.M. Smith, K.S. Novoselov, M.S. Skolnick, D.N. Krizhanovskii and A.I. Tartakovskii, *Nature Communications* **9**, 4797 (2018)
- [29] Jie Gu, V. Walther, L. Waldecker, D. Rhodes, A. Raja, J. C. Hone, T. F. Heinz, Stéphane Kéna-Cohen, Thomas Pohl, Vinod M. Menon, arXiv:1912.12544
- [30] M. Förg, L. Colombier, R. K. Patel, J. Lindlau, A. D. Mohite, H. Yamaguchi, M. M. Glazov, D. Hunger and A. Högele, *Nature Communications* **10**, 3697 (2019)
- [31] Z. Fei, M. E. Scott, D. J. Gosztola, J. J. Foley IV, J. Yan, D. G. Mandrus, H. Wen, P. Zhou, D. W. Zhang, Y. Sun, J. R. Guest, S. K. Gray, W. Bao, G. P. Wiederrecht, and X. Xu, *Phys. Rev. B* **94**, 081402(R) (2016).
- [32] Z. Sun, J. Gu, A. Ghazaryan *et al.*, *Nature Photon.* **11**, 491 (2017).
- [33] M. Sidler, P. Back, O. Cotlet *et al.*, *Nature Phys.* **13**, 255 (2017).
- [34] D. S. Citrin and J. B. Khurgin, *Phys. Rev. B* **68**, 205325 (2003).
- [35] J. Levinsen, Guangyao Li, and Meera M. Parish, *Phys. Rev. Research* **1**, 033120 (2019)
- [36] Fei Xue, Fengcheng Wu, Ming Xie, Jung-Jung Su, and A. H. MacDonald, *Phys. Rev. B* **94**, 235302 (2016)
- [37] Y. N. Gartstein, Xiao Li, and C. Zhang, *Phys. Rev. B* **92**, 075445 (2015)
- [38] J. B. Khurgin, *Optica* **2**, 740 (2015)
- [39] A. Krasnok, S. Lepeshov, and A. Alú, *Optic Express* **26**, 12 (2018)
- [40] S. Latini, E. Ronca, U. De Giovannini, Hannes Hübener and A. Rubio, *Nano Lett.* **19**, 3473 (2019).
- [41] D. Novko, K. Lyon, D. J. Mowbray, V. Despoja, (2021) in preparation.
- [42] See Supplemental Material at [URL] for more details on ...
- [43] M. S. Tomaš, *Phys. Rev. A* **51**, 2545 (1995)

- [44] V. Despoja, M. Šunjić, L. Marušić, Phys. Rev. B **80**, 075410 (2009)
- [45] D. Novko, M. Šunjić, V. Despoja, Phys. Rev. B **93**, 125413 (2016)
- [46] L. Hedin, Phys. Rev. **139**, A796 (1965)
- [47] G. Strinati, Phys. Rev. B **29**, 5718 (1984)
- [48] G. Onida, L. Reining, A. Rubio, Rev. Mod. Phys. **74**, 601 (2002)
- [49] Mark S. Hybertsen, Steven G. Louie, Phys. Rev. B **34**, 5390 (1986)
- [50] M. Rohlfing, S. G. Louie, Phys. Rev. Lett. **81**, 2312 (1998)
- [51] W. Hanke and L. J. Sham, Phys. Rev. Lett. **43**, 387 (1979)